Fostering Li-ion Conduction in Zr-Sn-Al-based Mid-Entropy NASICON Electrolyte

Pratiksha Gami[a], Asish Kumar Das[a], Manish Badole[a], Hari Narayanan Vasavan[a], Samriddhi Saxena[a], Neha Dagar[a], Sonia Deswal[b], Pradeep Kumar[b], Abhilash Dwivedi[c], Himanshu Kumar Poswal[c] and Sunil Kumar[a,d]*

[a]Department of Metallurgical Engineering and Materials Science, Indian Institute of Technology Indore, Simrol, 453552, India.

[b]School of Physical Sciences, Indian Institute of Technology Mandi, Himachal Pradesh, 175005, India.

[c]High Pressure & Synchrotron Radiation Physics Division, Bhabha Atomic Research Centre, Mumbai, 400085, India.

[d]Center for Electric Vehicle and Intelligent Transport Systems, Indian Institute of Technology Indore, Simrol, 453552, India.

*Corresponding author

Corresponding author E-mail: sunil@iiti.ac.in

Abstract

NASICON (Na Super Ionic CONductor) type materials are an important class of solid-state electrolytes due to their high ionic conductivity along with decent chemical and electrochemical stability. In this study, a medium-entropy $Li_{1.5}Zr_{1.0}Sn_{0.5}Al_{0.5}(PO_4)_3$ (LZSAP) ceramic electrolyte was prepared via a solid-state synthesis method. Rietveld refinement confirmed the rhombohedral structure of the conventionally sintered sample (LZSAP-CS) at 1000 °C. The spark plasma sintering (SPS) technique was used for the densification of the pellet and resulted in ~ 2.64 times higher room temperature conductivity (~ 4.42×10^{-5} S cm^{-1}) than that of the LZSAP-CS. The activation energy, calculated in the 30 – 100 °C range, decreased from 0.37 ± 0.01 eV for LZSAP to 0.31 ± 0.01 eV for LZSAP-CS. The transference number of Li^+ was ~0.98, indicating that Li^+ is the predominant charge carrier in this electrolyte. Further investigation of the lithium metal-electrolyte interface was conducted using a symmetric Li|LZSAP-SPS|Li cell configuration, demonstrating stability for over 500 h at 5 µA cm^{-2}. LZSAP extends the list of suitable solid-state electrolytes for all-solid-state lithium batteries.

Keywords: Electrochemistry**, s**olid electrolytes, NASICON, spark plasma sintering, ionic conductivity.

1. Introduction

The necessity for developing clean and effective energy conversion and storage technologies is driven by demands for enhancing energy security, halting climate change, and improving the environment [1, 2]. Due to their exceptional energy and power densities, lithium-ion batteries significantly enhance mobility and portability in society. [3, 4]. Combustible liquid electrolytes, however, may pose a safety risk with conventional lithium-ion batteries [5, 6]. Solid electrolytes (SEs) are a viable substitute for traditional organic liquid electrolytes, effectively mitigating safety problems [5, 7, 8]. Moreover, high-voltage cathodes and Li metal anodes can be used thanks to integrating solid electrolytes, substantially boosting the energy density of all-solid-state batteries (ASSBs) [7, 9-12].

All-solid-state batteries (ASSBs) are considered promising contenders for the next generation of energy storage devices and attract much attention. [13-15]. Much research has focused on finding SEs, including inorganic conductors, organic polymer electrolytes, and organic-inorganic composite electrolytes [16-20]. Polymer electrolytes, which are fabricated by dissolving lithium salts (i.e., Lithium bis(trifluoromethane sulfonyl)imide (LITFSI), Lithium bis(fluorosulfonyl)imide (LiFSI), etc.) in a polymer matrix, typically show flexibility and good interfacial contact with the cathodes/anodes [21, 22]. Poly (vinylidene fluoride-hexafluoropropylene)(PVDF-HFP) and Poly (ethylene oxide) (PEO) are examples of polymer matrices that have been extensively explored [23-27]. Unfortunately, low Li-ion transference numbers (~0.3), relatively low oxidation potential, and unsatisfactory ionic conductivity ($<10^{-6}$ S cm^{-1}) are common drawbacks for these polymers [22, 28, 29].

Inorganic conductors exhibit better thermal stability and moderate ion conductivity (>10^{-5} S cm^{-1} at RT) [30-32]. Additionally, since inorganic SEs are typically single-ion conductors, they can evade concentration polarization [19]. Batteries using ceramics-based inorganic electrolytes are well-suited for harsh operating conditions due to their inherently high elastic modulus [33-35]. Li-ion conducting inorganic electrolytes involving oxide-type, sulfide-type, halide-type, perovskites, etc., are widely documented and are good candidates for electrolytes in ASSBs [19, 31]. Among these, sulfur-type electrolytes possess extraordinarily high conductivities. Nevertheless, thiophosphate-based conductors are usually moisture-sensitive; they hydrolyze to produce hazardous H_2S gas, and the electrochemical stability window is also restricted [36, 37]. Direct exposure of sulfides to lithium metal or electrode materials results in significant redox changes [38, 39]. To rectify these issues, coating layers or interlayer protection are necessary [39]. Nonetheless, capacity decline is still witnessed in most cases [40]. Oxide electrolytes typically exhibit greater electrochemical and moisture stability but have less ionic conductivity than sulfides. NASICONs (i.e., $LiM_2(PO_4)_3$ where M = Zr, Ge, Sn, etc.) are intriguing electrolytes with a three-dimensional transport network that endows the framework with remarkable Li^+ conducting properties [41-45]. They also exhibit excellent chemical and thermal stability. This family is one of the few SE classes with high lithium-ion conducting properties and outstanding chemical/electrochemical stability [46, 47].

Over the last few years, the conducting behavior of oxide-type conductors has been dramatically enhanced *via* chemical substitution or implementation of additives [48, 49]. Both the framework bottleneck size and the Li^+ concentration were adjusted by substituting isovalent or heterovalent ions, and these changes affected the overall conductivity of the crystalline NaSICON-based Li^+ electrolytes [47]. Due to the significantly lower energy barrier, lithium ions migrate via a coordinated process rather than the single-ion hopping mechanism typically assumed [50]. It was observed that increased Li^+ concentration causes more coordinated migration, greatly enhancing lithium-ion conductivity [46, 50]. The Al-doped $LiGe_2(PO_4)_3$ (LGP) and $LiTi_2(PO_4)_3$ (LTP) materials have excellent Li^+ conductivity ($>10^{-4}$ S cm^{-1}), but Ge is quite costly, and the Ti in LTP-based materials get reduced when it comes into contact with metallic lithium [44, 51]. On the other hand, $LiZr_2(PO_4)_3$ (LZP), demonstrates excellent electrochemical stability with Li anode as the energy of the zirconium/zirconium-ion redox pair is greater than Li metal's Fermi level. However, it has comparatively lower room temperature (RT) ionic conductivity [45, 52, 53].

NASICON-type materials with multi-cations at the M-site are known to have better Li-ion diffusion owing to the stabilization of the rhombohedral phase at lower calcination temperatures [44, 48]. Due to their enhanced electrical and electrochemical performance, the high-entropy oxides (multiple cations at the M-site) with the NASICON framework have also drawn interest recently [54, 55]. One of the challenges with NASICON-structured is the anti-sintering behavior due to the anisotropic thermal expansion of the rhombohedral lattice during the sintering process. Accordingly, various techniques have such as, such as hot-press sintering, hot-isostatic press, microwave sintering, spark plasma sintering (SPS), etc., have been utilized to fabricate dense ceramics [56-59]. SPS provides notable advantages over other sintering methods, which include reduced processing times, lower temperatures, and, therefore, improved material properties [59, 60]. The short holding duration is appealing for research on Li^+ conductors since Li evaporation is unavoidable in protracted sintering processes at high temperatures, resulting in compositional inhomogeneities, impurity phase formation, and, consequently, reduced Li-ion conductivity [61]. Kobayashi et al. reported over 100 times improvement in room temperature Li-ion conductivity of

$LiTi_2(PO4)_3$ ceramics fabricated via the SPS [62]. Similar improvements in other functional properties have been reported in other classes of spark plasma sintered samples [63, 64].

In this work, a solid-state synthesis method was used to fabricate a medium entropy (S_{config} = 1.04R; here, R = Gas constant) $Li_{1.5}Zr_{1.0}Sn_{0.5}Al_{0.5}(PO_4)_3$ (LZSAP) sample and characterized using X-ray diffraction (XRD), field-emission scanning electron microscopy (FESEM), X-ray photoelectron spectroscopy (XPS), and electrochemical impedance spectroscopy (EIS) techniques. A dense LZSAP sample (relative density ~ 92%) fabricated using the spark plasma sintering (SPS) at 1000 °C showed a remarkable room temperature conductivity of 4.42×10^{-5} S cm^{-1}. Additionally, the symmetric cell made using the solid electrolyte sample showed excellent stability in lithium plating-stripping over 500 h.

2. Experimental Section

2.1. Pellet Fabrication

Polycrystalline LZSAP solid electrolyte was prepared using the traditional solid-state method. The materials used were lithium carbonate (Li_2CO_3), zirconium oxychloride octahydrate ($ZrOCl_2 \cdot 8H_2O$), tin oxide (SnO_2), aluminum nitrate nonahydrate ($Al(NO_3)_3 \cdot 9H_2O$), ammonium dihydrogen phosphate ($NH_4H_2PO_4$). The corresponding stoichiometric amounts of these materials were ground manually in mortar and pestle. An excess of 10% Li_2CO_3 was added to compensate for the lithium loss. In a box furnace, the material was preheated at 600 °C for 12 h, followed by ball milling for 6h. After that, the powder was pressed (~150 MPa) uniaxially to make pellets (~10 mm). The optimized sintering and calcination temperature was found by heating green ceramic discs at various temperatures. To reduce lithium loss during reactive sintering at temperatures above 950 °C, sacrificial powder was used to cover the pellets. The LZSAP samples were also sintered via SPS using the powders conventionally sintered at 1000 °C. Prior to SPS treatment, these pellets were homogenized by ball-milling them in acetone for 15 minutes at 200 rpm. Following drying, powders were put into a cylindrical graphite die (inner diameter of 20 mm). The residual graphite was eliminated using abrasive papers with grit numbers #150, #800, and finally #2000 to refine the sample surface, followed by decarburization at 600 °C and annealing at 800 °C.

2.2. Structural Analysis

The as-prepared ceramic samples were subjected to monochromatic Cu-kα radiation (2θ range: 10°–50°) in an Empyrean - Malvern Panalytical diffractometer to obtain X-ray diffraction (XRD) patterns. The XRD pattern was fitted utilizing the Rietveld refinement method with the TOPAS Academic (version 6) program to determine the lattice parameter and sample density [65]. Synchrotron XRD data for the LZSAP sample were collected over a temperature range of 50 to 550 °C, encompassing both heating and cooling cycles at the extreme condition X-ray diffraction (ECXRD) Beam Line (BL-11) at the Indus-2 synchrotron source, RRCAT, India. An X-ray beam with a wavelength of λ = 0.7301 Å was used. With the aid of an energy-dispersive X-ray spectrometer (EDS) linked to the FESEM (model: JEOL-7610+), the microstructures and elemental percentages of the ceramic pellets were determined. The XPS analysis was performed using a Thermofisher Scientific - Naxsa instrument base with a monochromated Al Kα X-ray source (1486.6 eV).

2.3. Electrical and Electrochemical Characterizations

The electrical conductivity of samples was measured in the 1 Hz - 1 MHz frequency band using an LCR meter (Make: NF Corp., ZM2376). The ceramic pellets were dried at 120 °C to eliminate residual moisture before the EIS measurements. The flat surfaces of each ceramic disk were covered with a layer of silver paste. The Nyquist plots were deconvoluted employing an appropriate equivalent circuit model using the EIS analyzer software [66]. Applying a DC polarization of 0.5 V across the sample, the electronic conductivity and Li^+ migration number were measured using chronoamperometry (Keithley Source Meter Unit: model 2450-EC). Symmetric Li|LZSAP|Li cells, using a ~ 1.5 mm thick SPS electrolyte, were assembled in a glovebox (H_2O & O_2: <0.1 ppm) to assess the stability of the LZSAP/Li interface.

3. Results and Discussion

3.1. Structural Analysis Results

The phase evolution at various temperatures of reactive sintering was confirmed using powder X-ray diffraction. The XRD patterns of fabricated LZSAP-*x* (*x* = 950 °C, 1000 °C, 1050 °C, and SPS) are shown in Fig. 1(a). The patterns indicate minor impurity phases of aluminum phosphate, tin oxide, and lithium phosphate, consistent with previous findings in the literature [67, 68]. Figure 1(b) illustrates the Rietveld refinement of the XRD data for the LZASP-1000 sample (hereafter referred to as LZSAP-CS). The pink-colored open circle symbols represent the experimental XRD data, whereas the blue-colored line displays the Rietveld refined profile. The solid grey line shows the difference curve, and the olive vertical bars show the calculated Bragg's peak positions for the space group $R\bar{3}c$. The background was refined using a 12-order polynomial function, and the peak was modeled utilizing the pseudo-Voigt II function (simple axial model) and sample displacement correction. The lattice parameters of the LZSAP phase were calculated to be $a = b = 8.7405(7)$ Å, $c = 21.8318(2)$ Å, and the unit cell volume was 1444.43(3) Å^3. In comparison, the lattice parameters for $LiZr_2(PO_4)_3$ are: $a = b = 8.8532(6)$ Å, $c = 22.2531(4)$ Å; V = 1510.18(1) Å^3. The effective ionic radius of the M-site for LZSAP is ~ 0.67 Å (octahedrally-coordinated - $r_{Zr^{4+}} = 0.72$ Å, $r_{Sn^{4+}} = 0.69$ Å, and $r_{Al^{3+}} = 0.535$ Å). As a result, the volume of the LZSAP unit cell is expected to be lesser than that of $LiZr_2(PO_4)_3$. This change in lattice parameters confirms the successful incorporation of Sn and Al in the unit cell. Here the values of R_{wp}(%) and R_p(%) are 10.663(2) and 7.6146(3), respectively. Table 1 provides the refined atomic coordinates, occupancy, and Wyckoff positions within the LZSAP-CS framework.

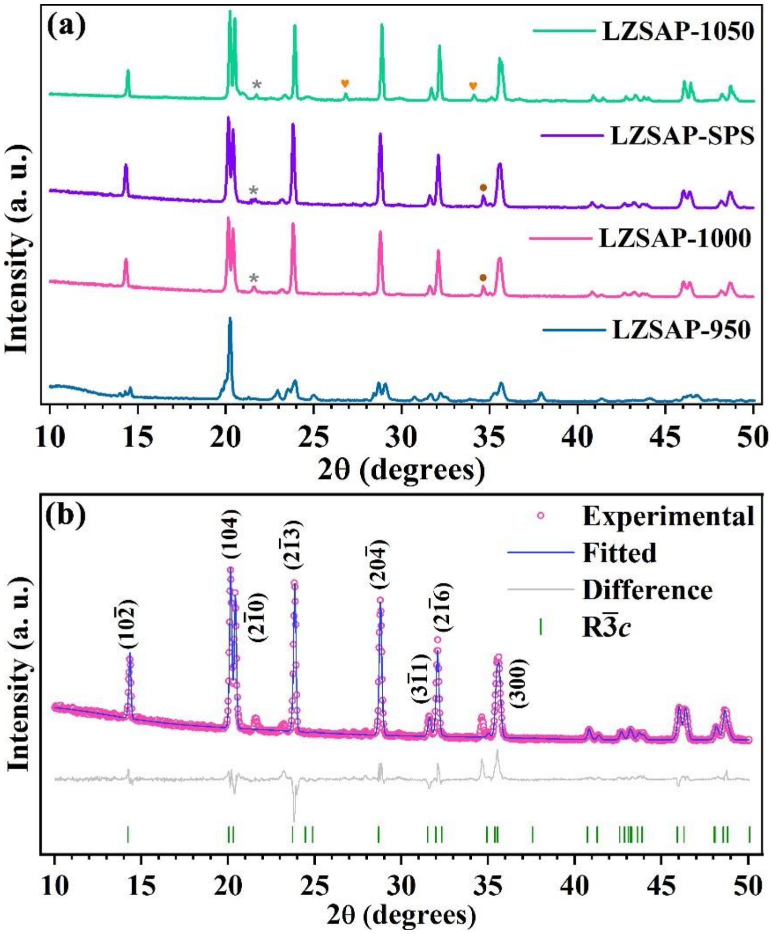

Fig.1. (a) RT XRD patterns at various reactive sintering temperatures in which the grey asterisk denotes $AlPO_4$, orange hearts indicate Li_3PO_4, and brown solid circle indicate peaks corresponding to minor SnO_2 impurity phases; (b) Rietveld refinement of RT XRD data of LZSAP-CS pellet. The experimental data is shown by a pink open circle; a blue line illustrates the fitted data; the difference is represented by a grey line and Bragg's peak position of the rhombohedral $R\bar{3}c$ space group is denoted by olive vertical bars.

As shown in Fig. S1(a), corner-sharing metal octahedra and phosphate tetrahedra form a crystalline framework with the rhombohedral ($R\bar{3}c$) symmetry, generating two unique Li sites (Li1-6*b*, Li2-36*f*). The phosphates and MO_6 polyhedra are alternated in a rhombohedral NASICON framework, creating 3D tunnels for better Li-ion mobility. The Li^+ transportation path across the LZSAP-CS framework was determined using the softBV program, using the CIF derived from the Rietveld refinement of the XRD data [69]. The output of the BVPA algorithm, plotted using the VESTA program, is displayed in Fig. S1(b). The 3D-linked Li-ion migration routes in LZSAP-CS are depicted in this figure.

Table 1 Various crystallographic parameters of LZSAP-CS obtained from the Rietveld refinement of RT powder XRD data.

Site	**Wyckoff position**	***x***	***y***	***z***	**Elements**	**Occupancy**
Li1	6*b*	0	0	0	Li^{+1}	1
Li2	36*f*	0	0.25	0.05	Li^{+1}	0.0833
Zr	12*c*	0	0	0.14(2)	Zr^{+4}	0.50
Al	12*c*	0	0	0.14(2)	Al^{+3}	0.25
Sn	12*c*	0	0	0.14(2)	Sn^{+4}	0.25
P	18*e*	0.29(3)	0	0.25	P^{+5}	1
O1	36*f*	0.19(8)	-0.04(9)	0.20(9)	O^{-2}	1
O2	36*f*	0.18(3)	0.13(5)	0.08(7)	O^{-2}	1

Temperature-dependent synchrotron powder XRD experiments were performed to estimate the thermal expansion of the LZSAP-SPS unit cell. Figure 2(a) shows the results during heating and cooling, from 50 to 550 °C with a temperature interval of 50 °C. Figures 2(b), 2(c), and 2(d) display magnified views of 2θ within the ranges 9.29°-9.72°, 14.75°-15.10°, and 23.96°-24.41°, respectively, as depicted in the contour plots. With the increase in temperature, there is a discernable shift in the 2θ positions of various peaks. For instance, the (104) peak (~ 9.45°) shifts toward a lower 2θ value with an increase in temperature (in the entire 50-550 °C range) and shifts to its original 2θ position upon decreasing the temperature back to 50 °C (Fig. 2(b)).

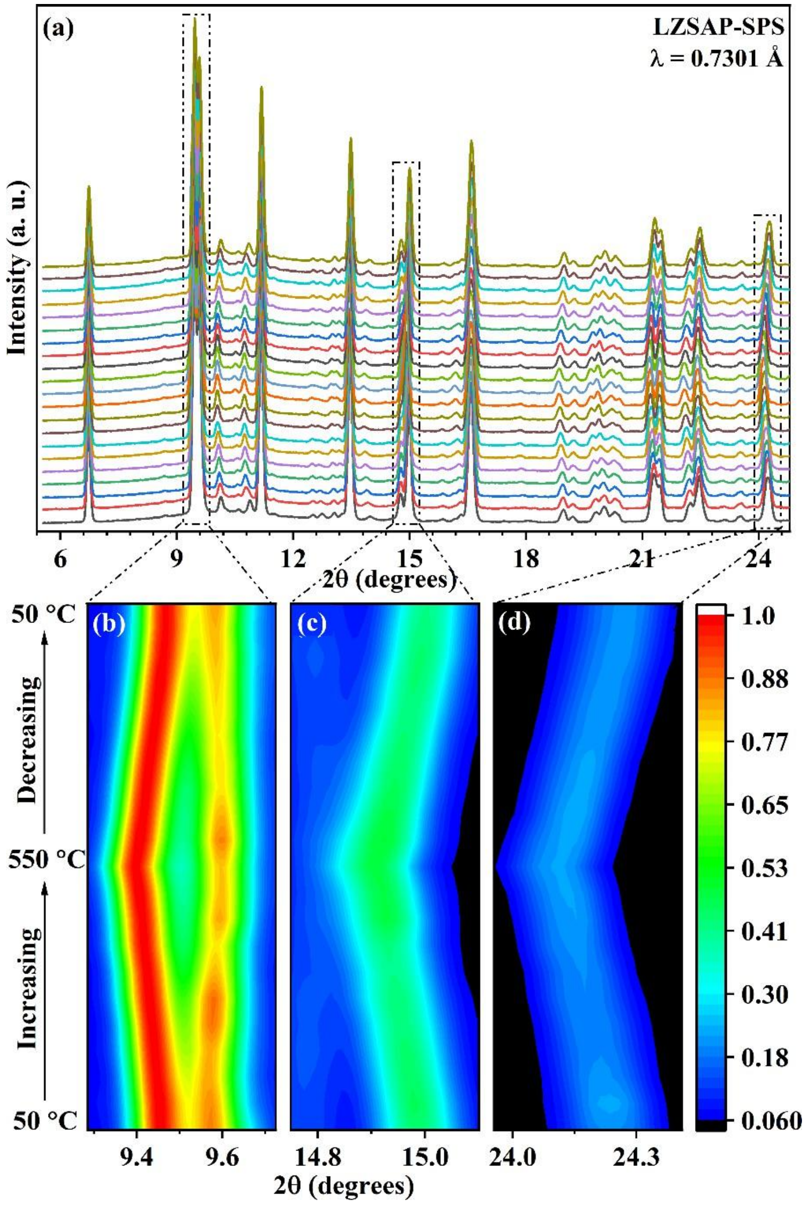

Fig. 2(a) displays the temperature-dependent synchrotron XRD pattern of LZSAP-SPS during the 50 - 500 °C heating-cooling cycle. To illustrate the reversible change in peak positions, the magnified view is displayed in contour plots 2(b), 2(c), and 2(d).

To quantify the changes in lattice parameters with temperature, Rietveld refinement of the temperature-dependent XRD data of the LSAZP-SPS sample at all temperatures was carried out, and the variation of the calculated lattice parameters with temperature (in the heating cycle) is shown in Fig. 3. The lattice parameter *'c'* increases, and '*a*' decreases linearly with the increase in temperature. In the temperature range from 50 to 550 °C, the thermal expansion coefficients for *'a'* and *'c'* are -4.28×10^{-6} and $+2.07 \times 10^{-5}$ K^{-1}, respectively. The anisotropic thermal expansion is known to cause anti-sintering behavior in several NASICON-type ceramics. The anisotropic thermal expansion causes stress at the grain boundaries (GBs) among unevenly aligned grains during cooling from high sintering temperatures, resulting in poor densification due to cracking [44, 70].

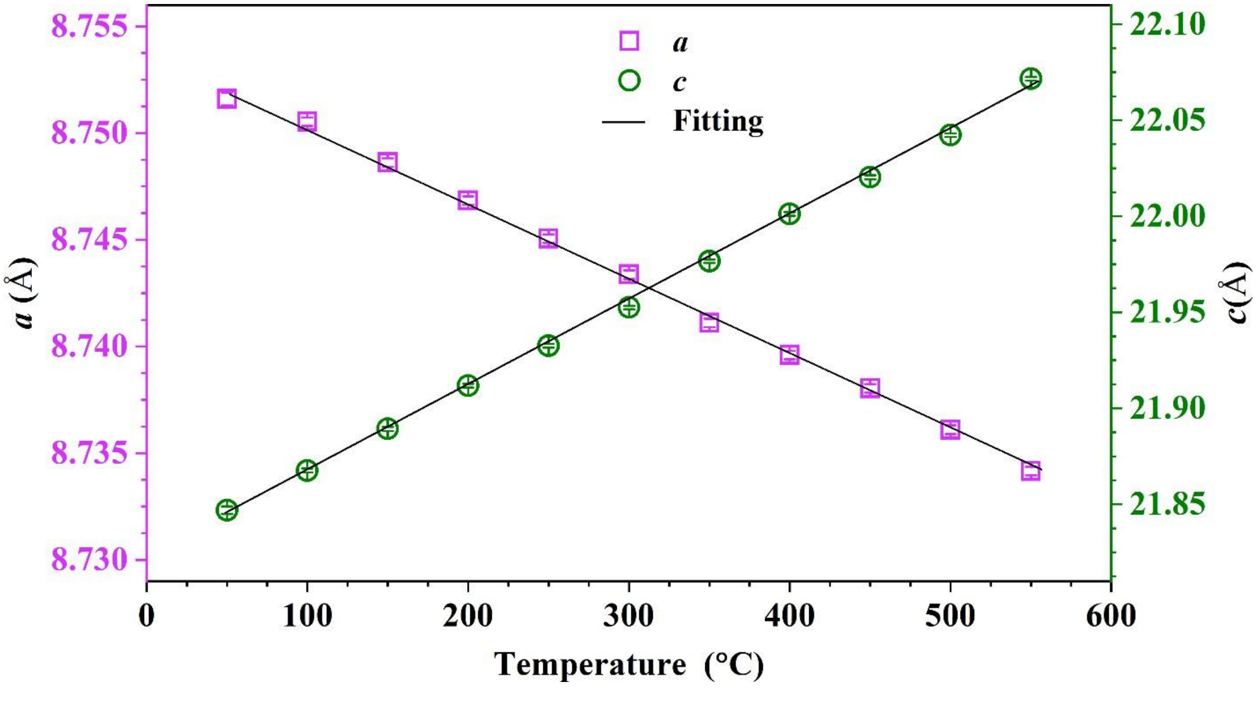

Fig. 3. Variations in lattice parameters (a and c) of the LZSAP-SPS sample at various temperatures, depicted with error bars.

SEM images of conventionally sintered (LSAZP-CS) and spark plasma sintered (LZSAP-SPS) samples are shown in Fig. 4. The LZSAP-CS pellet displays comparatively poor grain contact than the LZSAP-SPS pellet (Fig. 4(a) and 4(b)(inset)). The relative densities of LZSAP-CS and LZSAP-SPS pellets were ~ 82% and ~ 92%. The elements distribution of as-prepared LZSAP-SPS was ascertained by EDS elemental mapping (Fig. 4). The atomic % of the elements are shown in Table S1. The atoms Zr, Al, Sn, P, and O are homogeneously distributed among the sample, and there is no discernible elemental segregation in any of the samples. Further, no crack is visible in the SEM of LZSAP-SPS and LZSAP-CS, which may be attributed to low anisotropy in change of lattice parameters during cooling. Figures S2 and S3 show SEM images of LZSAP-950 and LZSAP-1050, respectively.

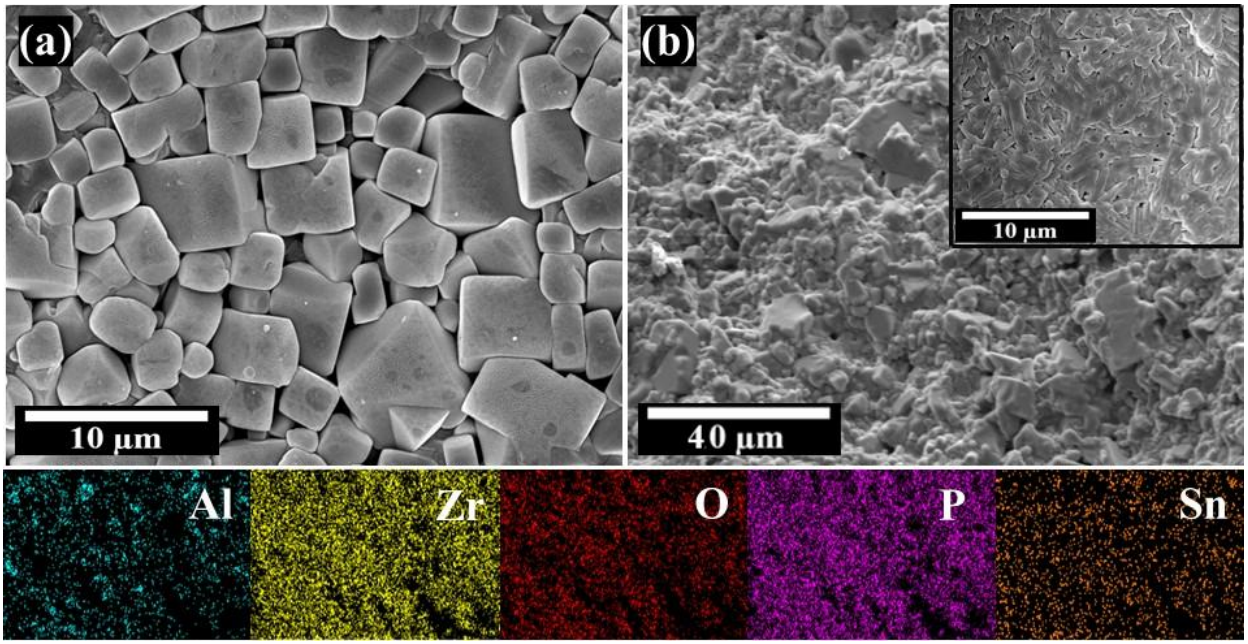

Fig. 4. SEM micrographs showing the surface morphology of (a) LZSAP-CS, (b) LZSAP-SPS (inset shows a magnified image at 10 µm scale), and EDS mappings of Al, Zr, O, P, and Sn elements present in the LZSAP-SPS sample.

The XPS spectra of Zr 3*d* & P 2*s*, Sn 3*d*, Al 2*p*, P 2*p*, and O 1*s*, along with their fitted profiles, are displayed in Fig. 5. The binding energy was calibrated using the hydrocarbon C 1*s* peak at 285 eV as the reference value. In Fig. 5(a), the Zr peak positions in the fitted spectrum are observed at

185.3 & 182.8 eV, corresponding to the Zr $3d_{3/2}$ & Zr $3d_{5/2}$. The Sn(3*d*) spectrum can be deconvoluted into two peaks at 495.5 & 487.1 eV, which are attributed to Sn $3d_{3/2}$ & Sn $3d_{5/2}$, respectively (Fig. 5(b)). This suggests that Sn and Zr are in a tetravalent state within the electrolyte. The Al(2*p*) spectrum shows a single peak at 74.9 eV, which indicates a +3 oxidation state for Al (Fig. 5(c)). Similarly, P $2p_{1/2}$ and P $2p_{3/2}$ peaks at 134.53 and 133.68 eV, respectively, typically supporting the presence of P^{+5} (Fig. 5(d)). The spin-orbit splitting (j-j coupling) for Zr(3*d*), Sn(3*d*), and P(2*p*) are 2.5 eV, 8.4 eV, and 0.85 eV, respectively. It is to be noted that the absence of a considerable asymmetry peak in the Sn(3*d*) XPS for LZSAP-SPS indicates the absence of Sn^{+2} in the sample [71, 72]. Figures 5(e) display the high-resolution XPS spectra of LZSAP for the O 1*s* at 531.6 eV.

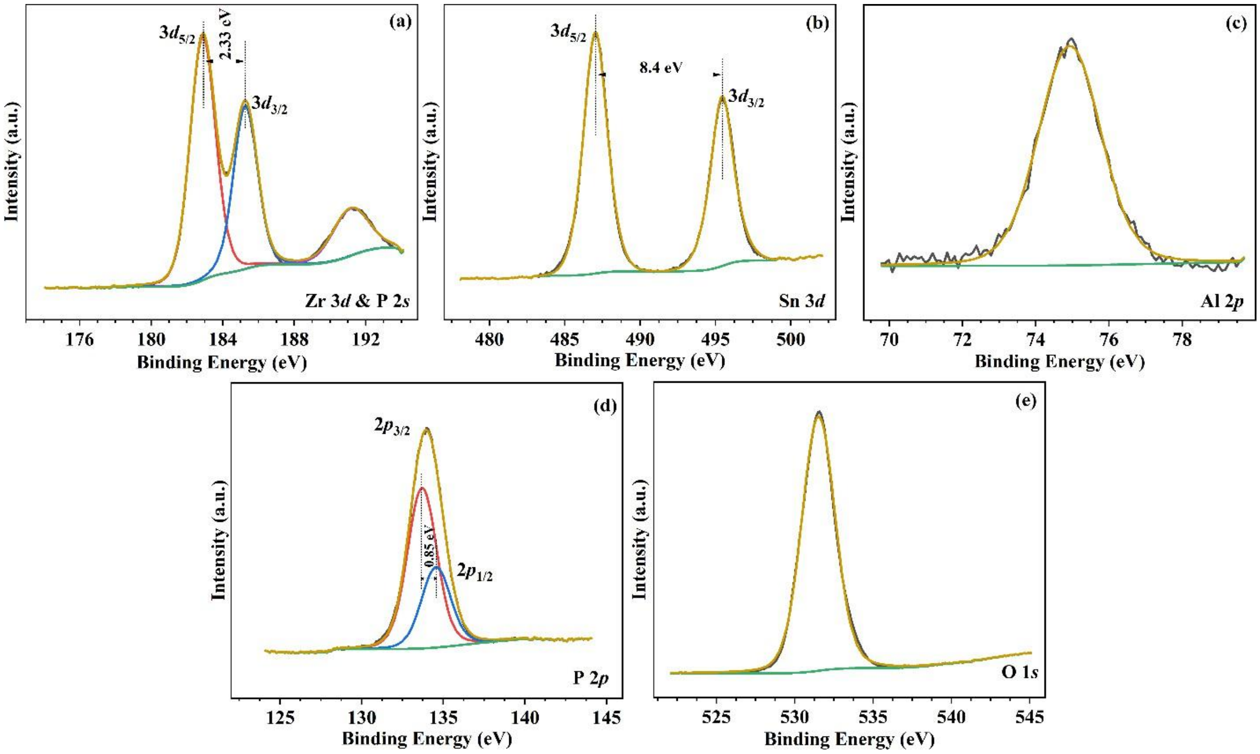

Fig. 5. The fitted XPS data of (a) Zr 3d & P 2s, (b) Sn 3d, (c) Al 2p, (d) P 2p, and (e) O 1s of LZSAP-SPS.

3.2. Electrical and Electrochemical Analysis Result

Impedance spectroscopy was used to evaluate the electrolyte's kinetic properties from 1 MHz to 1 Hz. The complex impedance spectra (Fig. 6 and S4) were recorded using silver as blocking electrodes, and total resistance was calculated by fitting the impedance data using EIS analyzer software [73]. The data observed for the conventionally sintered samples were fitted utilizing the corresponding equivalent circuit demonstrated in Fig. 6 inset, where Q is the constant phase element (subscripts *ep*, *g*, and *gb* represent electrode polarization, grain/bulk, and grain boundary, respectively), R represents the total resistance, R_g is for grain, and R_{gb} is for grain boundary resistance. Nyquist plots of LZSAP-SPS and LZSAP-1050, at high frequencies, have a single semi-circular arc that represents the total resistance (Fig. 6(b) and S4(b)). The occurrence of ion-blocking electrode polarization causes the slanted line observed in the low-frequency area. As illustrated in Fig. S4(a), LZSAP heated to 950 °C demonstrated the lowest total room temperature (RT) conductivity (6.56×10^{-8} S cm^{-1}) among the conventionally sintered ceramics. The LZSAP-CS and LZSAP-950 samples displayed two overlapping semicircular arcs (Figs. 6(a) and S4(a)). The first arc in the lower frequency region correlates to grain boundary resistance, while the second arc in a relatively higher frequency region indicates grain resistance. The slanted line at low frequencies corresponds to the electrode contact resistance at the Ag/electrolyte interface.

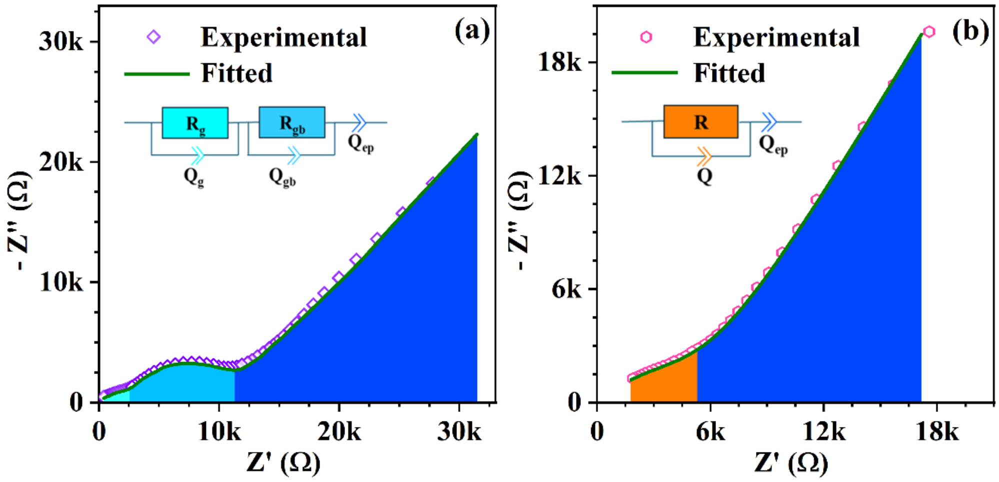

Fig. 6. RT Nyquist plots of (a) LZSAP-CS and (b) LZSAP-SPS with corresponding equivalent circuits for fitting the spectra.

LZSAP-950 and LZSAP-CS samples had bulk conductivity of 2.31 × 10^{-6} S cm^{-1} and 4.85 × 10^{-5} S cm^{-1}, respectively, whereas the grain boundary conductivities were 9.17 × 10^{-7} S cm^{-1} and 2.55 × 10^{-5} S cm^{-1}. In comparison, the fitted total conductivity values of the LZSAP-CS and LZSAP-SPS samples are 1.67 × 10^{-5} S cm^{-1} and 4.42 × 10^{-5} S cm^{-1}, respectively, which are both inferior to those of LZSAP-950 and LZSAP-1050 due to presence of impurity phases.

Figure 7 illustrates the temperature-dependent total conductivity (σ) of LZSAP-CS and LZSAP-SPS. The Arrhenius equation ($\sigma = \sigma_0 \exp(-E_a/k_BT)$, where σ_0 is the pre-exponential factor, and k_B is the Boltzmann constant) was used to model the data. The LZSAP-SPS sample had a lower activation energy (E_a), around 0.31 ± 0.01 eV, compared to the LZSAP-CS sample (0.37 ± 0.01 eV). The calculated activation energy value is within the range of values documented for fast lithium-ion conductors based on rhombohedral NASICON architecture [41, 74]. LZSAP-SPS exhibits better ionic conduction at different temperatures due to its reduced activation energy and better densification. The presence of pores at the grain boundaries or at triple points impedes the Li-ion conduction not just by increasing the overall diffusion length but also by creating localized inhomogeneous current densities in the vicinity of these pores [62, 75].

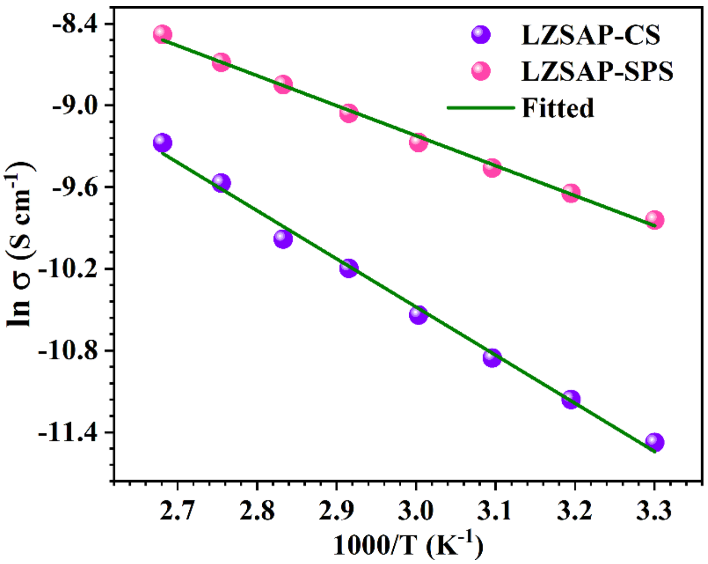

Fig. 7. Arrhenius plots of LZSAP-CS and LZSAP-SPS samples.

To assess the contribution of lithium-ion to total electrical conduction in the LZSAP-SPS sample, a DC polarization investigation was executed with silver serving as the blocking electrode [76]. The current variation over time following a DC polarization of 0.5 V across the Ag|LZSAP-SPS|Ag pellet is shown in Fig. 8. In the NASICON ceramic electrolytes, no anionic conduction due to the immobile $(PO_4)^{3-}$ is expected to contribute to the RT conductivity due to its large size and strong bonding. Therefore, the current I_t-I_e is due to the Li-ion motion, where I_t stands for initial current (contributions from both electronic & ionic motion) and I_e for steady-state current (only electronic charge carriers are responsible for the steady-state current since the silver electrode block Li^+ at the sample-electrode interface). The Li-ion transference number ($t_{Li}{}^+$), calculated using the formula $t_{Li}{}^+ = 1-(I_e/I_t)$, was found to be around 0.98, confirming the LZSAP to be a predominant Li^+ conductor.

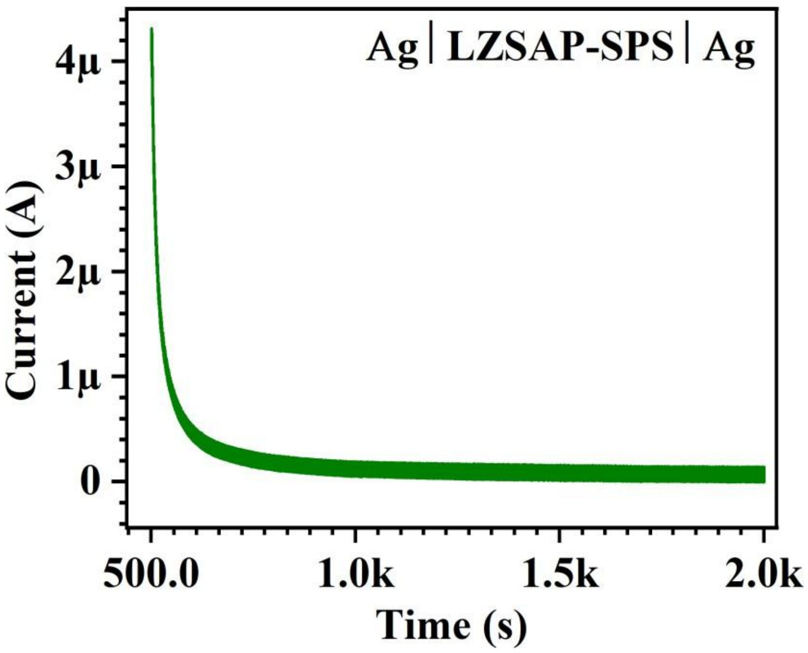

Fig. 8. Chronoamperometry profile at 0.5 V for Ag|LZSAP-SPS|Ag.

A symmetric Li|LZSAP-SPS|Li battery configuration was congregated to investigate the stability and Li-ion migration at the lithium/electrolyte junction at RT. Figure S5 displays the Nyquist plot of the symmetric cell. The Li/LZSAP interfacial resistance (~ 65 kΩ) dominates the overall resistance of the cell, not the solid electrolyte's bulk resistance. When the symmetric battery was cycled at 5 µA cm^{-2} (Fig. 9), the overpotential increased from ~ 0.3 V for the fresh cell to ~0.5 V at the end of the 500th cycle. This increase in resistance indicates a continuous growth in the passivation layer at the Li/LZSAP interface. Upon decrimping the cycled cell, the LZSAP-SPS pellet's surface was darker, suggesting a chemical interaction between the Li metal and the LZSAP electrolyte (Fig. S6). To reduce the interfacial resistance, a lithium-alloy cushioning or organic polymer layer is needed to prevent direct contact between lithium metal and solid electrolyte, which is under investigation.

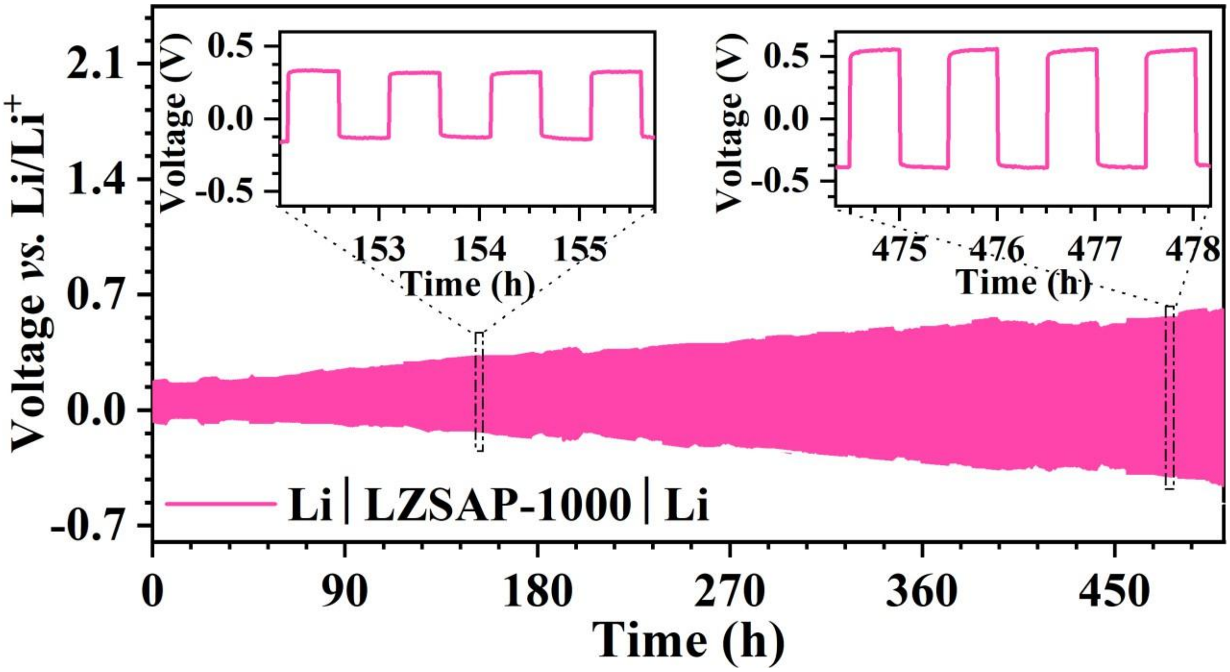

Fig. 9. Li metal plating-stripping test of Li/LZSAP-SPS/Li symmetric cell at the current density of 5 µA cm^{-2} at RT. The insets are the magnified view of the voltage profile at different periods.

4. Conclusions

In summary, the addition of Al^{3+} for Sn^{4+} in $LiZrSn(PO_4)_3$ preserves the Li^+ conducting rhombohedral NASICON-framework at RT and enhances the Li-ion concentration in the unit cell. Temperature-dependent synchrotron XRD data confirm the anisotropic thermal expansion with a small decrease in the lattice parameter '*a'* and a much increase in lattice parameter '*c'* with increasing temperature. The total ionic conductivity of LZSAP-SPS at RT was 4.42×10^{-5} S cm^{-1} with an associated activation energy of 0.31 ± 0.01 eV. The Li^+ transference number was ~0.98, indicating that Li^+ is the primary charge carrier in the LZSAP electrolyte. The Li/electrolyte junction is further studied with symmetric Li|LZSAP-SPS|Li battery testing, which showed only a marginal increase in the overpotential over 500 h. These findings should pave the way for further studies on NASICON-type electrolytes and their potential use in all-solid-state lithium batteries.

Declaration of competing interest

The authors declare that they have no known competing financial interests or personal relationships that could have appeared to influence the work reported in this paper.

Acknowledgments

SK thanks the Science and Engineering Research Board (SERB) for the Core Research Grant (Grant no. CRG/2021/005548). Department of Science and Technology (DST), Government of India is also gratefully acknowledged for funding (Grant no. DST/TMD/IC-MAP/2K20/01).

Data availability

Data will be made available on request.

References

[1] M. Armand, J.M. Tarascon, Building better batteries, Nature, 451 (2008) 652-657.

[2] C. Ling, A review of the recent progress in battery informatics, npj Computational Materials, 8 (2022) 33.

[3] T.-H. Kim, J.-S. Park, S.K. Chang, S. Choi, J.H. Ryu, H.-K. Song, The Current Move of Lithium Ion Batteries Towards the Next Phase, Adv. Energy Mater., 2 (2012) 860-872.

[4] K. Xu, Electrolytes and Interphases in Li-Ion Batteries and Beyond, Chem. Rev., 114 (2014) 11503-11618.

[5] J.B. Goodenough, K.S. Park, The Li-ion rechargeable battery: a perspective, J. Am. Chem. Soc., 135 (2013) 1167-1176.

[6] M.S. Whittingham, Lithium Batteries and Cathode Materials, Chem. Rev., 104 (2004) 4271-4302.

[7] Y.-S. Hu, Batteries: Getting solid, Nat. Energy, 1 (2016) 16042.

[8] N. Kamaya, K. Homma, Y. Yamakawa, M. Hirayama, R. Kanno, M. Yonemura, T. Kamiyama, Y. Kato, S. Hama, K. Kawamoto, A. Mitsui, A lithium superionic conductor, Nat. Mater., 10 (2011) 682-686.

[9] Y. Hu, W. Li, J. Zhu, S.-M. Hao, X. Qin, L.-Z. Fan, L. Zhang, W. Zhou, Multi-layered electrolytes for solid-state lithium batteries, Next Energy, 1 (2023) 100042.

[10] C. Yang, K. Fu, Y. Zhang, E. Hitz, L. Hu, Protected Lithium-Metal Anodes in Batteries: From Liquid to Solid, Adv. Mater., 29 (2017) 1701169.

[11] C. Sun, J. Liu, Y. Gong, D.P. Wilkinson, J. Zhang, Recent advances in all-solid-state rechargeable lithium batteries, Nano Energy, 33 (2017) 363-386.

[12] B. Scrosati, Recent advances in lithium ion battery materials, Electrochim. Acta, 45 (2000) 2461-2466.

[13] J.C. Barbosa, R. Gonçalves, C.M. Costa, S. Lanceros-Méndez, Toward Sustainable Solid Polymer Electrolytes for Lithium-Ion Batteries, ACS Omega, 7 (2022) 14457-14464.

[14] L. Wang, J. Li, G. Lu, W. Li, Q. Tao, C. Shi, H. Jin, G. Chen, S. Wang, Fundamentals of Electrolytes for Solid-State Batteries: Challenges and Perspectives, Frontiers in Materials, 7 (2020).

[15] M.J. Lee, J. Han, K. Lee, Y.J. Lee, B.G. Kim, K.-N. Jung, B.J. Kim, S.W. Lee, Elastomeric electrolytes for high-energy solid-state lithium batteries, Nature, 601 (2022) 217-222.

[16] P. Verma, P. Maire, P. Novák, A review of the features and analyses of the solid electrolyte interphase in Li-ion batteries, Electrochim. Acta, 55 (2010) 6332-6341.

[17] S.S. Zhang, A review on electrolyte additives for lithium-ion batteries, J. Power Sources, 162 (2006) 1379-1394.

[18] Q. Zhao, S. Stalin, C.Z. Zhao, L.A. Archer, Designing solid-state electrolytes for safe, energy-dense batteries, Nat. Rev. Mater., 5 (2020) 229-252.

[19] P. Knauth, Inorganic solid Li ion conductors: An overview, Solid State Ion., 180 (2009) 911-916.

[20] L. Fan, S. Wei, S. Li, Q. Li, Y. Lu, Recent Progress of the Solid-State Electrolytes for High-Energy Metal-Based Batteries, Adv. Energy Mater., 8 (2018).

[21] J. Li, Y. Cai, H. Wu, Z. Yu, X. Yan, Q. Zhang, T.Z. Gao, K. Liu, X. Jia, Z. Bao, Polymers in Lithium-Ion and Lithium Metal Batteries, Adv. Energy Mater., 11 (2021).

[22] Y. An, X. Han, Y. Liu, A. Azhar, J. Na, A.K. Nanjundan, S. Wang, J. Yu, Y. Yamauchi, Progress in Solid Polymer Electrolytes for Lithium-Ion Batteries and Beyond, Small, 18 (2022).

[23] Y. Jiang, X. Yan, Z. Ma, P. Mei, W. Xiao, Q. You, Y. Zhang, Development of the PEO based solid polymer electrolytes for all-solid state lithium ion batteries, Polymers, 10 (2018).

[24] A.K. Das, M. Badole, H.N. Vasavan, S. Saxena, P. Gami, S. Kumar, Highly conductive ceramic-in-polymer composite electrolyte enabling superior electrochemical performance for all-solid-state lithium batteries, Ceram. Int., 49 (2023) 29719-29728.

[25] A.K. Das, M. Badole, H.N. Vasavan, S. Saxena, P. Gami, S. Deswal, P. Kumar, S. Kumar, Enhancing room temperature performance of solid-state lithium cell via a facile solid electrolyte-cathode interface design, Mater. Today Sustain., 26 (2024) 100758.

[26] A.K. Das, M. Badole, H.N. Vasavan, S. Saxena, P. Gami, N. Dagar, S. Kumar, Integrated cathode-electrolyte ($Li_{6.55}La_3Zr_{1.55}Ta_{0.45}O_{12}$/PEO-LiTFSI) architecture driven excellent performance of solid-state lithium metal batteries, Journal of Energy Storage, 94 (2024) 112452.

[27] S.A. Ahmed, T. Pareek, S. Dwivedi, M. Badole, S. Kumar, Fast Li^+ conduction in ($PEO+LiClO_4$) incorporated $LiSn_2(PO_4)_3$ polymer-in-ceramic solid electrolyte, AIP Conference Proceedings, 2265 (2020).

[28] Y. Zhao, L. Wang, Y. Zhou, Z. Liang, N. Tavajohi, B. Li, T. Li, Solid Polymer Electrolytes with High Conductivity and Transference Number of Li Ions for Li-Based Rechargeable Batteries, Advanced Science, 8 (2021).

[29] A.K. Das, M. Badole, H.N. Vasavan, S. Saxena, P. Gami, N. Dagar, S. Kumar, $LiTa_2PO_8$-Based Polymer–Ceramic Electrolyte Paved the Way to High-Performance Solid-State Lithium Metal Batteries, Energy & Fuels, (2024).

[30] M. Shoji, E.J. Cheng, T. Kimura, K. Kanamura, Recent progress for all solid state battery using sulfide and oxide solid electrolytes, J. Phys. D: Appl. Phys., 52 (2019).

[31] F. Liang, Y. Sun, Y. Yuan, J. Huang, M. Hou, J. Lu, Designing inorganic electrolytes for solid-state Li-ion batteries: A perspective of LGPS and garnet, Mater. Today, 50 (2021) 418-441.

[32] M. Irfan, M. Atif, Z. Yang, W. Zhang, Recent advances in high performance conducting solid polymer electrolytes for lithium-ion batteries, J. Power Sources, 486 (2021).

[33] C. Wang, J.T. Kim, C. Wang, X. Sun, Progress and Prospects of Inorganic Solid-State Electrolyte-Based All-Solid-State Pouch Cells, Adv. Mater., (2023).

[34] V. Raj, N.P.B. Aetukuri, J. Nanda, Solid state lithium metal batteries – Issues and challenges at the lithium-solid electrolyte interface, Curr. Opin. Solid State Mater. Sci., 26 (2022).

[35] Y.Y. Sun, Q. Zhang, L. Yan, T.B. Wang, P.Y. Hou, A review of interfaces within solid-state electrolytes: fundamentals, issues and advancements, Chem. Eng. J., 437 (2022).

[36] Z. Liu, W. Fu, E.A. Payzant, X. Yu, Z. Wu, N.J. Dudney, J. Kiggans, K. Hong, A.J. Rondinone, C. Liang, Anomalous High Ionic Conductivity of Nanoporous β-Li_3PS_4, J. Am. Chem. Soc., 135 (2013) 975-978.

[37] Y. Seino, T. Ota, K. Takada, A. Hayashi, M. Tatsumisago, A sulphide lithium super ion conductor is superior to liquid ion conductors for use in rechargeable batteries, Energy & Environmental Science, 7 (2014) 627-631.

[38] T. Swamy, X. Chen, Y.-M. Chiang, Electrochemical Redox Behavior of Li Ion Conducting Sulfide Solid Electrolytes, Chem. Mater., 31 (2019) 707-713.

[39] G.F. Dewald, S. Ohno, M.A. Kraft, R. Koerver, P. Till, N.M. Vargas-Barbosa, J. Janek, W.G. Zeier, Experimental Assessment of the Practical Oxidative Stability of Lithium Thiophosphate Solid Electrolytes, Chem. Mater., 31 (2019) 8328-8337.

[40] M. Ma, M. Zhang, B. Jiang, Y. Du, B. Hu, C. Sun, A review of all-solid-state electrolytes for lithium batteries: high-voltage cathode materials, solid-state electrolytes and electrode–electrolyte interfaces, Materials Chemistry Frontiers, 7 (2023) 1268-1297.

[41] T. Pareek, S. Dwivedi, M. Badole, S. Kumar, On processing structure–conductivity relations in NASICON-type $LiSn_2(PO_4)_3$, Bull. Mater. Sci., 44 (2021) 177.

[42] M. Hou, F. Liang, K. Chen, Y. Dai, D. Xue, Challenges and perspectives of NASICON-type solid electrolytes for all-solid-state lithium batteries, Nanotechnology, 31 (2020) 132003.

[43] G.F. Ortiz, M.C. López, P. Lavela, C. Vidal-Abarca, J.L. Tirado, Improved lithium-ion transport in NASICON-type lithium titanium phosphate by calcium and iron doping, Solid State Ion., 262 (2014) 573-577.

[44] D. Safanama, N. Sharma, R.P. Rao, H.E.A. Brand, S. Adams, Structural evolution of NASICON-type $Li_{1+x}Al_xGe_{2-x}(PO_4)_3$ using in situ synchrotron X-ray powder diffraction, J. Mater. Chem., 4 (2016) 7718-7726.

[45] Y. Zhang, K. Chen, Y. Shen, Y. Lin, C.W. Nan, Enhanced lithium-ion conductivity in a $LiZr_2(PO_4)_3$ solid electrolyte by Al doping, Ceram. Int., 43 (2017).

[46] K. Singh, A. Chakraborty, R. Thirupathi, S. Omar, Recent advances in NASICON-type oxide electrolytes for solid-state sodium-ion rechargeable batteries, Ionics, 28 (2022) 5289-5319.

[47] I. Stenina, S. Novikova, D. Voropaeva, A. Yaroslavtsev, Solid Electrolytes Based on NASICON-Structured Phosphates for Lithium Metal Batteries, Batteries, 9 (2023).

[48] Q. Zhou, B. xu, P.-H. Chien, Y. Li, B. Huang, N. Wu, H. Xu, N. Grundish, Y.Y. Hu, J. Goodenough, NASICON $Li_{1.2}Mg_{0.1}Zr_{1.9}(PO_4)_3$ Solid Electrolyte for an All-Solid-State Li-Metal Battery, Small Methods, 4 (2020) 2000764.

[49] V. Ramar, S. Kumar, S.R. Sivakkumar, P. Balaya, NASICON-type La^{3+} substituted $LiZr_2(PO_4)_3$ with improved ionic conductivity as solid electrolyte, Electrochim. Acta, 271 (2018) 120-126.

[50] H. Xie, Y. Li, J.B. Goodenough, NASICON-type $Li_{1+2x}Zr_{2-x}Ca_x(PO_4)_3$ with high ionic conductivity at room temperature, RSC Adv., 1 (2011) 1728-1731.

[51] H. Yamamoto, M. Tabuchi, T. Takeuchi, H. Kageyama, O. Nakamura, Ionic conductivity enhancement in $LiGe_2(PO_4)_3$ solid electrolyte, J. Power Sources, 68 (1997) 397-401.

[52] X. Pu, X. Cheng, Q. Yan, Y. Lin, R. Yan, R. Yang, X. Zhu, NASICON-type Ta^{5+} substituted $LiZr_2(PO_4)_3$ with improved ionic conductivity as a prospective solid electrolyte, Ceram. Int., 50 (2024) 9007-9015.

[53] I. Hanghofer, B. Gadermaier, A. Wilkening, D. Rettenwander, H.M.R. Wilkening, Lithium ion dynamics in $LiZr_2(PO_4)_3$ and $Li_{1.4}Ca_{0.2}Zr_{1.8}(PO_4)_3$, Dalton Trans., 48 (2019) 9376-9387.

[54] M. Botros, J. Janek, Embracing disorder in solid-state batteries, Science, 378 (2022) 1273-1274.

[55] Y. Feng, L. Yang, Z. Yan, D. Zuo, Z. Zhu, L. Zeng, Y. Zhu, J. Wan, Discovery of high entropy garnet solid-state electrolytes via ultrafast synthesis, Energy Storage Mater., 63 (2023) 103053.

[56] M. Kotobuki, H. Lei, Y. Chen, S. Song, C. Xu, N. Hu, J. Molenda, L. Lu, Preparation of thin solid electrolyte by hot-pressing and diamond wire slicing, RSC Adv., 9 (2019) 11670-11675.

[57] S. Patra, V. Krupa B R, S. Chakravarty, R. Murugan, Microstructural engineering in lithium garnets by hot isostatic press to cordon lithium dendrite growth and negate interfacial resistance for all solid state battery applications, Electrochimica Acta, 312 (2019) 320-328.

[58] Y. Yan, S. Li, J. Zhang, Z. Li, G. Ye, Z. Wang, Research on the Application of Internet of Things in Operation and Management of Distribution Sub-stations, 2020 5th International Conference on Power and Renewable Energy, ICPRE 2020, 2020, pp. 356-360.

[59] M. Kotobuki, M. Koishi, High conductive Al-free Y-doped $Li_7La_3Zr_2O_{12}$ prepared by spark plasma sintering, J. Alloys Compd., 826 (2020).

[60] G.B. Kunshina, O.O. Shichalin, A.A. Belov, E.K. Papynov, I.V. Bocharova, O.B. Shcherbina, Properties of $Li_{1.3}Al_{0.3}Ti_{1.7}(PO_4)_3$ Lithium-Conducting Ceramics Synthesized by Spark Plasma Sintering, Russ. J. Electrochem., 59 (2023) 173-181.

[61] X. Wei, J. Rechtin, E.A. Olevsky, The Fabrication of All-Solid-State Lithium-Ion Batteries via Spark Plasma Sintering, Metals, 2017.

[62] Y. Kobayashi, T. Takeuchi, M. Tabuchi, K. Ado, H. Kageyama, Densification of $LiTi_2(PO_4)_3$-based solid electrolytes by spark-plasma-sintering, Journal of Power Sources, 81-82 (1999) 853-858.

[63] M. Nižňanský, K. Vanmeensel, J. Vleugels, V. Tyrpekl, M. Vilémová, Review on high-pressure spark plasma sintering and simulation of the impact of die/punch material combinations on the sample temperature homogeneity, Open Ceramics, 16 (2023) 100433.

[64] M. Tokita, Progress of Spark Plasma Sintering (SPS) Method, Systems, Ceramics Applications and Industrialization, Ceramics, 2021, pp. 160-198.

[65] A.A. Coelho, TOPAS and TOPAS-Academic: an optimization program integrating computer algebra and crystallographic objects written in C++, J. Appl. Crystallogr., 51 (2018) 210-218.

[66] A.S.B.a.G.A. Ragoisha, EIS Spectrum Analyser, 2008.

[67] H. Jodi, Z. Supardi, E. Kartini, A. Zulfia, SYNTHESIS AND ELECTROCHEMICAL CHARACTERIZATION OF Li_3PO_4 FOR SOLID STATE ELECTROLYTES, Jurnal Sains Materi Indonesia, 16 (2016) 1-8.

[68] P. Goj, B. Handke, P. Stoch, Vibrational characteristics of aluminum–phosphate compounds by an experimental and theoretical approach, Scientific Reports, 12 (2022) 17495.

[69] H. Chen, L.L. Wong, S. Adams, SoftBV - a software tool for screening the materials genome of inorganic fast ion conductors, Acta Crystallogr B Struct Sci Cryst Eng Mater, 75 (2019) 18-33.

[70] J. Ibañez, C. Pecharroman, R. Jimenez, P. Duran-Martin, M.G. Lazarraga, J.M. Rojo, Microstructure and Ionic Conductivity of $LiSn_2P_3O_{12}$-Teflon Composites, J. Electrochem. Soc., 148 (2001) J31.

[71] H. Li, L. Guo, X. Liu, T. Sun, Q. Li, F. Zhang, G. Xiao, T. Fu, Y. Chen, High Temperature Conductive Stability of Indium Tin Oxide Films, Frontiers in Materials, 7 (2020).

[72] T. Pareek, S. Dwivedi, B. Singh, D. Kumar, P. Kumar, S. Kumar, $LiSnZr(PO_4)_3$: NASICON-type solid electrolyte with excellent room temperature Li^+ conductivity, J. Alloys Compd., 777 (2019) 602-611.

[73] J.T.S. Irvine, D.C. Sinclair, A.R. West, Electroceramics: Characterization by Impedance Spectroscopy, Adv. Mater., 2 (1990) 132-138.

[74] S. Kumar, P. Balaya, Improved ionic conductivity in NASICON-type Sr^{2+} doped $LiZr_2(PO_4)_3$, Solid State Ion., 296 (2016) 1-6.

[75] K. Waetzig, A. Rost, C. Heubner, M. Coeler, K. Nikolowski, M. Wolter, J. Schilm, Synthesis and sintering of $Li_{1.3}Al_{0.3}Ti_{1.7}(PO_4)_3$ (LATP) electrolyte for ceramics with improved Li^+ conductivity, Journal of Alloys and Compounds, 818 (2020) 153237.

[76] V. Thangadurai, W. Weppner, Determination of the sodium ion transference number of the Dion-Jacobson-type layered provskite $NaCa_2Nb_3O_{10}$ using ac impedance and dc methods, Chem. Mater., 14 (2002) 1136-1143.

[Supplementary Material]

Fostering Li-ion Conduction in Zr-Sn-Al-based Mid-Entropy NASICON Electrolyte

Pratiksha Gami[a], Asish Kumar Das[a], Manish Badole[a], Hari Narayanan Vasavan[a], Samriddhi Saxena[a], Neha Dagar[a], Sonia Deswal[b], Pradeep Kumar[b], Abhilash Dwivedi[c], Himanshu Kumar Poswal[c] and Sunil Kumar[a,d]*

[a]Department of Metallurgical Engineering and Materials Science, Indian Institute of Technology Indore, Simrol, 453552, India.

[b]School of Physical Sciences, Indian Institute of Technology Mandi, Himachal Pradesh, 175005, India.

[c]High Pressure & Synchrotron Radiation Physics Division, Bhabha Atomic Research Centre, Mumbai, 400085, India.

[d]Center for Electric Vehicle and Intelligent Transport Systems, Indian Institute of Technology Indore, Simrol, 453552, India.

*Corresponding author

Corresponding author E-mail: sunil@iiti.ac.in

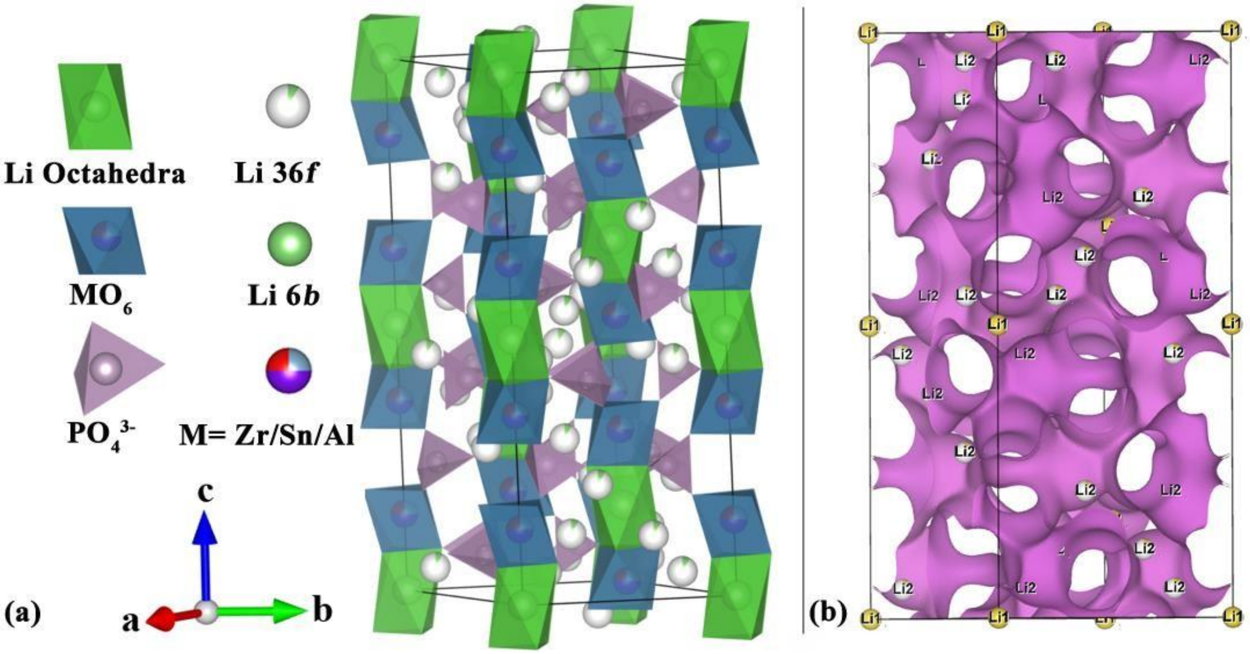

Fig. S1. (a) The crystal structure for LZSAP-CS and (b) Li-ion diffusion paths in the rhombohedral crystal structure of LSAZP-1050 are shown in three dimensions using blue isosurfaces that were produced using BVPA software.

Table S1: The atomic % of the various elements from the EDS analysis.

Elements (Experimental)	**Atomic (%)**
Sn	~ 2.6
Al	~ 2.4
Zr	~ 5.2
P	~ 14.8
O	~ 75

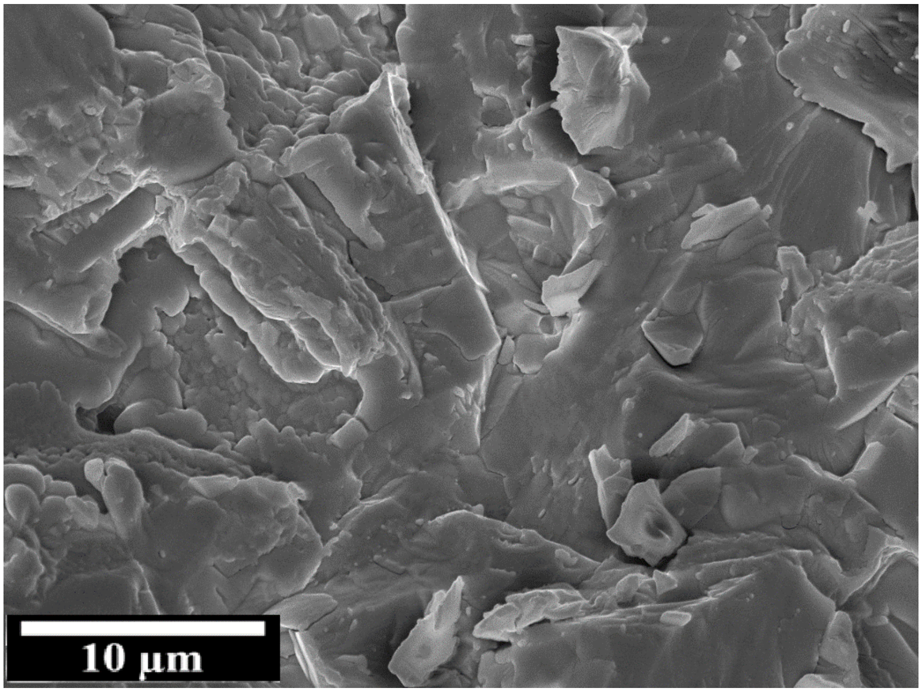

Fig. S2. SEM image of LZSAP-950.

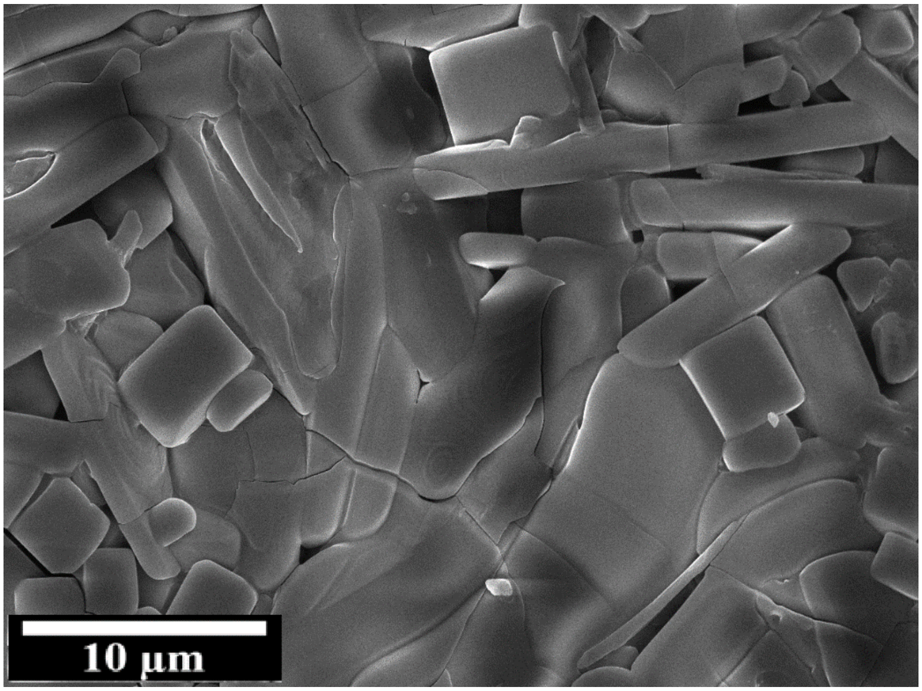

Fig. S3. SEM image of LZSAP-1050.

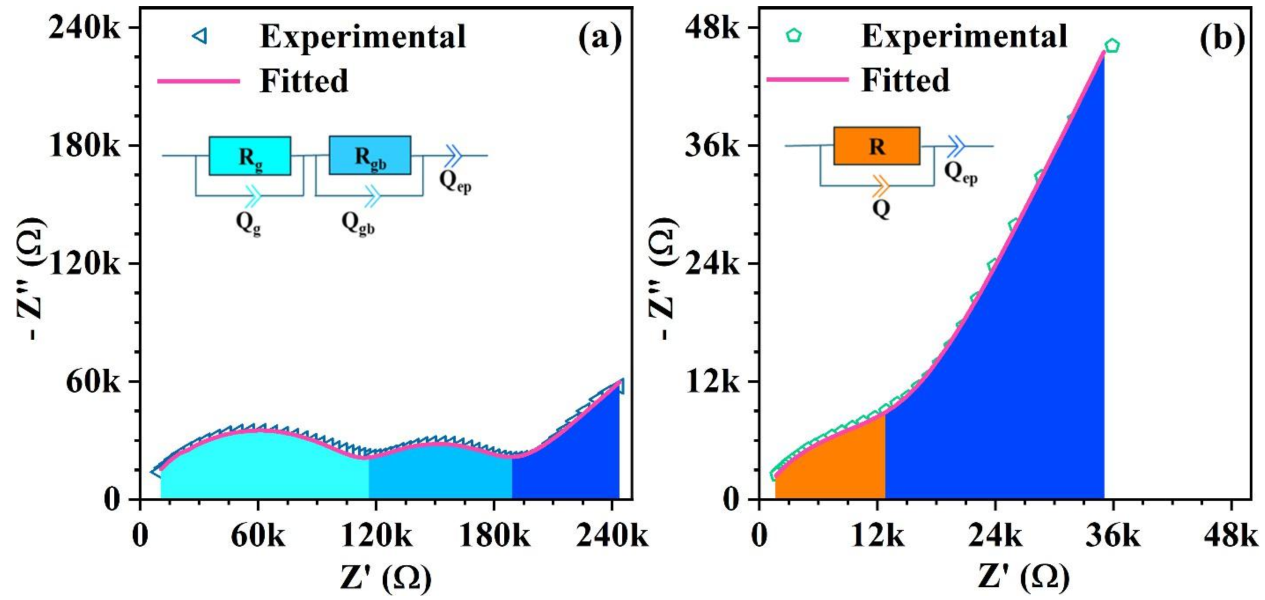

Fig. S4. RT Nyquist plots of (a) LZSAP-950 and (b) LZSAP-1050 with corresponding equivalent circuits for fitting the spectra.

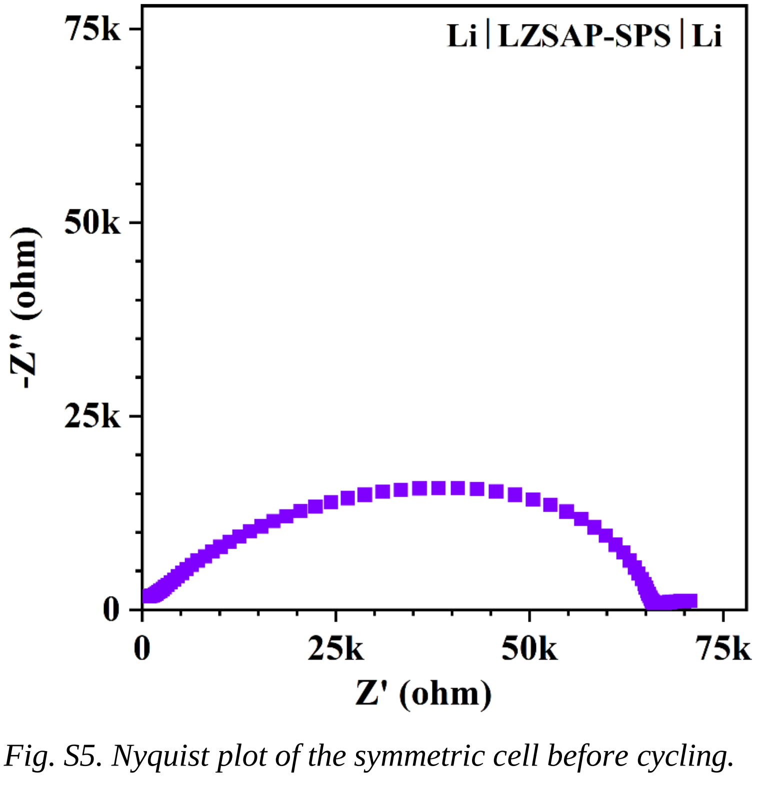

Fig. S5. Nyquist plot of the symmetric cell before cycling.

Fig. S6. Image of lithium metal after 500 cycles.